communications physics

Article

https://doi.org/10.1038/s42005-024-01642-5

Orbital-overlap-driven hybridization in 3d-transition metal perovskite oxides $LaMO_3$ (M = Ti-Ni) and La_2CuO_4

Chun-Yu Liu[1,2] ✉, Lorenzo Celiberti[3], Régis Decker[1], Kari Ruotsalainen[1], Katarzyna Siewierska[1], Maximilian Kusch[1], Ru-Pan Wang[4], Dong Jik Kim[5], Israel Ibukun Olaniyan[5,6], Daniele Di Castro[7,8], Keisuke Tomiyasu[9,10], Emma van der Minne[11], Yorick A. Birkhölzer[11], Ellen M. Kiens[11], Iris C. G. van den Bosch[11], Komal N. Patil[12], Christoph Baeumer[11], Gertjan Koster[11], Masoud Lazemi[12], Frank M. F. de Groot[12], Catherine Dubourdieu[5,6], Cesare Franchini[3,13] & Alexander Föhlisch[1,2] ✉

The wide tunability of strongly correlated transition metal (TM) oxides stems from their complex electronic properties and the coupled degrees of freedom. Among the perovskite oxides family, $LaMO_3$ (M = Ti-Ni) allows an M-dependent systematic study of the electronic structure within the same-structure-family motif. While most of the studies have been focusing on the 3d TMs and oxygen sites, the role of the rare-earth site has been far less explored. In this work, we use resonant inelastic X-ray scattering (RIXS) at the lanthanum $N_{4,5}$ edges and density functional theory (DFT) to investigate the hybridization mechanisms in $LaMO_3$. We link the spatial-overlap-driven hybridization to energetic-overlap-driven hybridization by comparing the RIXS chemical shifts and the DFT band widths. The scope is extended to highly covalent Ruddlesden-Popper perovskite La_2CuO_4 by intercalating lanthanum atoms to rock-salt layers. Our work evidences an observable contribution of localized lanthanum 5p and 4f orbitals in the band structure.

Transition metal (TM) perovskite oxides [ABO_3, A = rare earth (RE) cation, B = TM cation] are canonical strongly correlated ternary oxides. They have drawn considerable scientific interest due to their rich phase diagrams resulting from coupled orbital, spin, lattice, and charge degrees of freedom[1–10]. Consequently, the transport, magnetic, and optical properties can be tuned by, e.g., doping, strain, temperature or external fields, which bring about their functionalities. Their wide applications include catalysis[11–13], energy storage[14], and electronic devices[15,16] to name a few.

One of the factors that underlies the rich tunable physical properties is the orbital overlap[17,18]. Most of the studies of ABO_3 have focused on the oxygen and TM sites, which are the dominant components of the valence band maxima and the conduction band minima[19–23]. For example, e_g orbital mixing is the key to understanding the spin-, and orbital-order transition in manganites[24]. The 4f states of trivalent RE are generally considered to be highly localized due to the relativistic contraction[25–28]. Indeed, RE elements are often treated merely as geometric structure modulators or charge reservoirs in the context of complex oxides[1,29]. However, it has recently been suggested the RE 5d or 4f orbitals can be electronically hybridized with TM 3d[30–32]. The role of the RE has started to gain attention from the infinite layer nickelates where the hybridization between RE 5d and Ni 3d could have an influence on the Fermi surface and magnetic exchange[27,33–36]. In fact, it is still under debate how RE is participating in the hybridization scheme[37] and whether nickelates possess similar superconducting mechanisms in comparison to the cuprates[38,39].

[1]Institute for Methods and Instrumentation for Synchrotron Radiation Research, Helmholtz-Zentrum Berlin für Materialien und Energie GmbH, Berlin, Germany. [2]Institut für Physik und Astronomie, Universität Potsdam, Potsdam, Germany. [3]University of Vienna, Faculty of Physics and Center for Computational Materials Science, Vienna, Austria. [4]Institute for Nanostructure and Solid State Physics, Hamburg University, Hamburg, Germany. [5]Institute Functional Oxides for Energy-Efficient IT, Helmholtz-Zentrum Berlin für Materialien und Energie GmbH, Berlin, Germany. [6]Freie Universität Berlin, Physical and Theoretical Chemistry, Berlin, Germany. [7]Dipartimento di Ingegneria Civile e Ingegneria Informatica, Università di Roma Tor Vergata, Roma, Italy. [8]CNR-SPIN, Università di Roma Tor Vergata, Roma, Italy. [9]Department of Physics, Tohoku University, Sendai, Japan. [10]Nissan ARC Limited, Yokosuka, Japan. [11]MESA+ Institute for Nanotechnology, University of Twente, Faculty of Science and Technology, Enschede, The Netherlands. [12]Materials Chemistry and Catalysis, Debye Institute for Nanomaterials Science, Utrecht University, Utrecht, The Netherlands. [13]Department of Physics and Astronomy 'Augusto Righi', Alma Mater Studiorum - Università di Bologna, Bologna, Italy. ✉e-mail: chun-yu.liu@helmholtz-berlin.de; alexander.foehlisch@helmholtz-berlin.de

The lanthanum perovskite oxides $LaMO_3$ (M = Ti-Ni) are paradigmatic strongly correlated transition-metal oxides in which the physical properties are dominated by the partially filled d-states: from antiferromagnetic (AFM) Mott insulator to AFM charge-transfer insulator (TM = Ti-Fe), then to paramagnetic narrow gap insulator $LaCoO_3$, and finally to correlated metal $LaNiO_3$[40,41]. Several theoretical approaches were dedicated to bridging the relationship between electronic, geometric, and magnetic structures[42–45]. The key frontier orbitals that determine the functionalities are mainly TM 3d, O 2p and their degree of hybridization[46–48]. Locally, the TM^{3+} is coordinated by 6 O^{2-} in an octahedron and La^{3+} is coordinated by 12 O^{2-} and intercalated in the cubic unit cell [Fig. 1(a)]. The TM 3d orbitals hybridize with the O 2p[47] and the hybridization can be found as a general feature of 3d TM oxides[48]. Higher TM 3d - O 2p hybridization results in a delocalization of 3d electrons, an enhanced covalency, a lower on-site Coulomb interaction, a higher hopping term, and a broader band width. Covalency, which is associated with the hopping term in Hubbard model has a direct impact on the superexchange, which is a crucial parameter to determine the alignment of spins. For example, an ionic framework fails to describe magnetism in cuprates where covalency is significant between Cu and O[49]. However, the degree of involvement of La orbitals in the hybridization scheme remains ambiguous.

Resonant inelastic X-ray scattering (RIXS) is a spectroscopic technique capable of probing the electronic structure and the elementary excitations of a material[50]. The coherent second-order optical process is element- and orbital-selective and has delivered important insights on a wide range of functional materials, including transition metal oxides, quantum materials, and correlated metals[51–55]. Final states with constant energy loss represent an intrinsic excitation energy. A schematic excitation of charge and orbital is illustrated in Fig. 1b.

In this work, we revisit the TM perovskite oxides hybridization scheme from the perspective of the rare-earth site. We present high-resolution RIXS experiments at the La $N_{4,5}$-edges and determine the energy positions of the $^3D_1$ state ($5p^54f^1$ configuration) in $LaMO_3$ (M = Ti-Ni) and La_2CuO_4. We observe chemical shifts and we link them to the spatial and energetic overlap between TM 3d and La 4f, O 2s and La 5p. By combining the spectroscopic observables with first-principle density functional theory (DFT) calculations, we evidence the electronic hybridization between La and TM in perovskite oxides. The coupling mechanisms between La, TM, and O atoms are explained with intra- and interatomic orbital hybridizations.

Results

Figure 1a depicts an illustrative perovskite crystal structure and relative positions of the atoms in a $LaMO_3$. The excitation and radiative decay channels are shown in Fig. 1b. Two X-ray absorption (XAS) features similar to those reported in Ref. 56 are observed, which correspond to the $^3D_1$ and $^3P_1$ intermediate states. Due to being well self-screened, these two multiplet features show no observable chemical sensitivity. If we resonantly excite the electrons to the intermediate $^3D_1$ ($4d^94f^1$) state, three main radiative decay pathways are possible: (a) Elastic channel: The excited electrons relax back to the ground state. (b) Charge transfer (CT) channel: Electrons from O 2p shell refill the transient La 4d core hole. (c) Inner valence channel: A 5p electron decays via electric dipole transition and refills a 4d hole. The latter appears as a multiplet structure in the spectrum, which corresponds to atomic multiplets of the $5p^54f^1$ configuration[56–58]. The present study exploits the chemical shifts of the energetically lowest multiplet due to the change of the chemical environment along the 3d TM perovskite oxide series.

Indeed, it has been recently evidenced that these multiplets show chemical sensitivity, which indicates that hybridizations involving La 5p and 4f atomic orbitals affect the final state energy[56]. In a free-ion picture, the $^3D_1$ state is the only pure state while the rest of the multiple states are mixed of terms to some degree[59]. Previously, the $^3D_1$ energy positions in a wide range of La-containing systems were determined by the $LaAlO_3$ empirical model[56]. As described in Ref. 56, this model consists of a double-Voigt fit where the energy distances, the relative intensity ratios, and the intrinsic lifetime broadening are constrained and chemical broadenings are coupled. We apply this model to the perovskite compounds investigated in this work

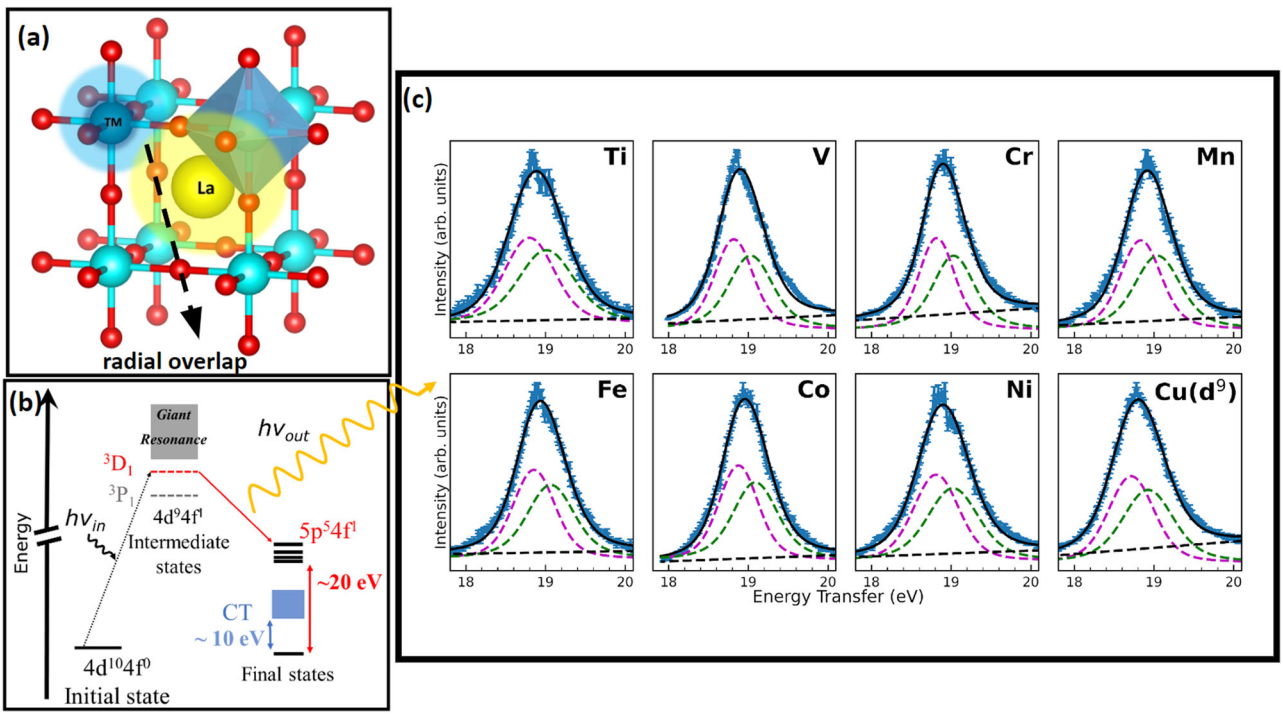

Fig. 1 | Resonant inelastic X-ray scattering (RIXS) process in perovskite oxides. **a** General lanthanum perovskite oxide structure and scheme of orbital overlap based on radial wave functions. TM represents transition metal ion. **b** Scheme of the X-ray absorption and RIXS process in La. $^3D_1$ and $^3P_1$ depict the atomic terms of $4d^94f^1$ electronic configuration. Charge transfer between ligands and metal centers is denoted as CT. **c** High-resolution RIXS spectra and fitted result. The purple- and green-dashed curves represent the $^3D_1$ and $^3D_2$ RIXS final states (electronic configuration $5p^54f^1$), respectively. The error bars are defined by the square root of the cumulative photon counts.

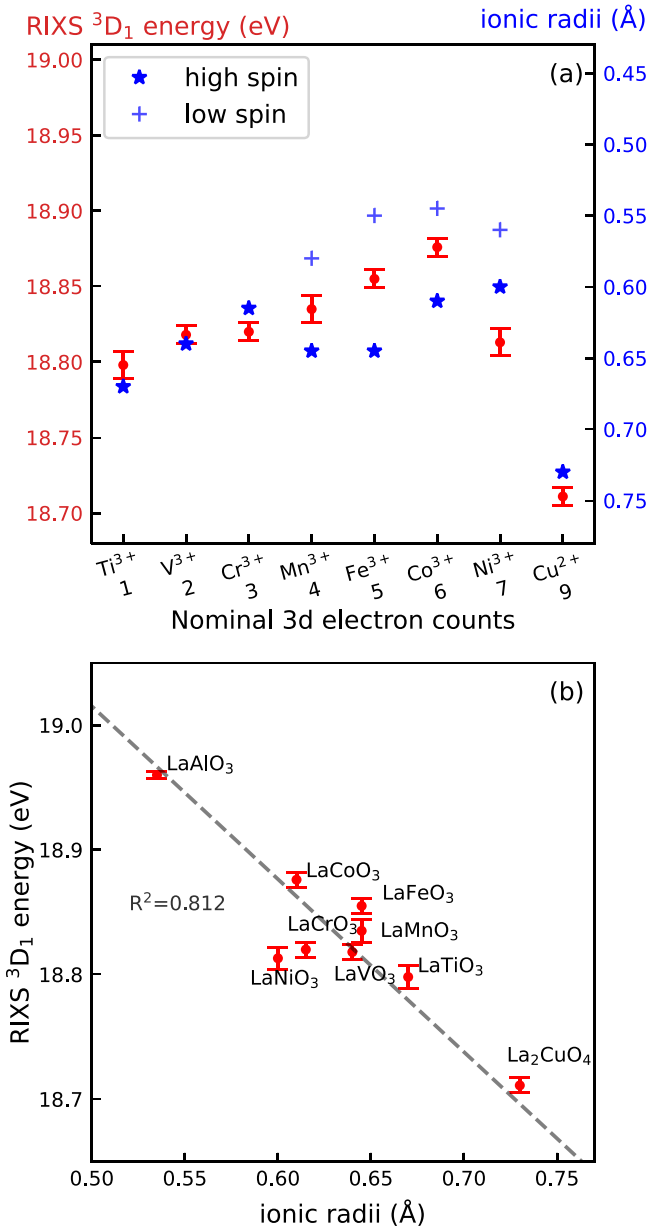

Fig. 2 | Resonant inelastic X-ray scattering (RIXS) chemical shifts and their correlation to transition metal (TM) ionic radii. a RIXS $^3D_1$ energy and TM ionic radii as a function of nominal 3d electron counts. Note that the axis of the ionic radii is plotted inversely. **b** Negative correlation between RIXS $^3D_1$ energy and TM (and Al^{3+}) ionic radii in perovskite oxides and Ruddlesden-Popper La_2CuO_4. We define the error bars as three times the standard errors[80] obtained from the model fits. Dashed linear regression line serves as a guide to the eye. High-spin ionic radii are selected for panel (b).

[Fig. 1c]. The model captures the lineshapes and determines the energy positions of the $^3D_1$ RIXS final state. Moderate differences in the peak widths (0.175 – 0.268 eV, details are listed in supplementary Table S1) are attributed to different degrees of chemical broadening. We note that strain and temperature have a marginal influence on the La RIXS shift (See supplementary Fig. S1).

Figure 2a shows the energy of the $^3D_1$ peak (in red) with respect to the nominal 3d electron counts on the TM site. By comparing the structurally similar perovskites, we first observe an increase of the peak energy when increasing n from $n = 1$ (Ti^{3+}) to $n = 6$ (Co^{3+}), i.e. when the 3d shell is half filled. From $n = 6$ to $n = 9$, as the 3d orbitals become doubly occupied and a pronounced decrease is observed. The evolution of the $^3D_1$ peak energy vs. the number of 3d electrons is put in perspective with the TM ionic radii in Fig. 2a in blue. The effective ionic radii are based on an octahedral crystal field with a coordination number of six[60]. As the ionic radii are strongly dependent on the local spin configuration, both high and low spin configuration radii are shown. On one hand, as the atomic number increases, the increasing attractive Coulomb interaction between nuclei and electrons will contract the radial wave function, which shrinks the ionic radius. On the other hand, the increasing unpaired spin expands the radial distribution of the electrons. These two aspects contribute to the monotonic increase of the $^3D_1$ peak energy with the decreasing ionic radii shown in Fig. 2b. We especially highlight the highly covalent Ruddlesden-Popper cuprate La_2CuO_4 where the overlap between TM and La is further enhanced by reduced charge and intercalation of La in the rock-salt layer. We also note the fact that Co^{3+} lies on the turning point, indicating that the highest ionicity (lowest covalency) between La-TM might correlate with the optimal cathode potential in Li-ion batteries[61].

In the following, we use density functional theory (DFT) calculations of the element- and orbital-resolved density of states (DOS) in combination with our experimental measurements in order to thoroughly understand the different intra- and interatomic hybridizations at play in $LaMO_3$.

Covalency is defined as the wavefunction overlap integral divided by the energy difference[62,63]. By constraining the geometric structure, coordination number and varying the 3d electron numbers, we compare both spatial-overlap-driven covalency (Experiment) and energetic-overlap-driven covalency (Theory). A larger spatial orbital overlap is generally associated with a higher hopping term, which leads to a broader band. The results of our approach are summarized in Fig. 3.

From an energetic overlap perspective, our DFT calculations first show a clear energetic overlap of the La 4f with TM 3d from Ti to Mn ($n = 1$–4). Moving on to late TMs, the 4f band isolates from the 3d band. In addition, TM 3d orbitals hybridize with the O 2p orbitals, which further intra-atomically hybridize with O 2s, also known as O sp^3 hybrid orbitals. At last, the O 2s and La 5p orbitals hybridize as they lie close to each other in terms of energies. We note that even though La RIXS at $N_{4,5}$ edges does not directly probe the La 5d orbitals, intra-atomic 4f-5d hybridization was proposed earlier[64,65]. Therefore we cannot exclude the La 5d - La 4f mechanism from the RIXS chemical shift. From crystal field's perspective, La 5d - O 2p interaction is expected to be larger than the TM 3d - O 2p due to the extended radial distribution. Likewise, we cannot exclude the La 5d - TM 3d (O 2p) - La 4f hybridization pathways.

Orbital hybridization modifies the effective on-site Coulomb repulsion U and hopping term t under Hubbard model. Hence, the hybridization is associated with the band width. To further address the degree of hybridization, we analyze the La 5p and 4f band widths (W_p and W_f, respectively), extracted from the projected density of states by taking the energy difference between the top and bottom edges of the La 5p and 4f peaks respectively. In particular, states below 2% of the peaks maxima are neglected. First, we plot the sum of the W_p and W_f against RIXS energy [Fig. 4a]. The trend in $W_p + W_f$ along the 3d TM series is akin to the $^3D_1$ RIXS energy. Figure 4b displays how the W_p and W_f evolve across the TM series: When going from early TM to late TM, the 4f band shrinks, indicative of a more localized character, while the La 5p band expands, indicative of a more itinerant character. This can be partially rationalized by the increasing effective nuclear charge of the TM. Heavier TM will shrink the effective ionic radius, which decreases the overlap with the La 4f band. Therefore, while in early TM perovskites the TM 3d band has moderate overlap with the La 4f band, the La 4f starts to localize when going to late TM. This trend can be linked back to the experimental observations: as the TM ionic radius decreases, the 3d orbital wave function has less overlap with the La 4f wave function. Finally, we examine the layered perovskite La_2CuO_4 which has an even higher orbital overlap and a larger ionic radius due to the nominal charge Cu^{2+} and Ruddlesden-Popper structure. The increase in band widths and RIXS red shift of La_2CuO_4 observed in Fig. 4 further indicate high La-Cu covalency besides the well-known Cu-O covalency. However, it is still unclear whether it is the structure change or the ionic radius change that has more contribution in the RIXS redshift.

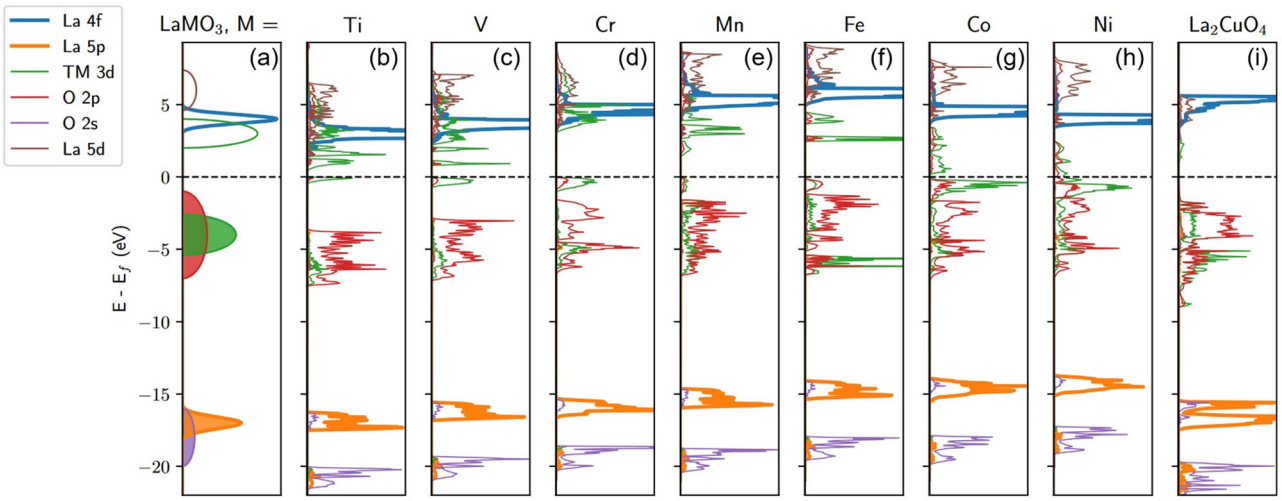

Fig. 3 | Summary of the calculated density of states (DOS). a Schematic view of the projected DOS. The elements, atomic orbitals, and their relative energy levels as well as distributions are illustrated. **b–i** Calculation results of $LaMO_3$ (M = Ti-Ni respectively) and La_2CuO_4. La 4f (in blue) and La 5p (in orange) are highlighted in thicker line width and are used for the following band width analysis. TM denotes transition metal. The Fermi level is denoted as E_f.

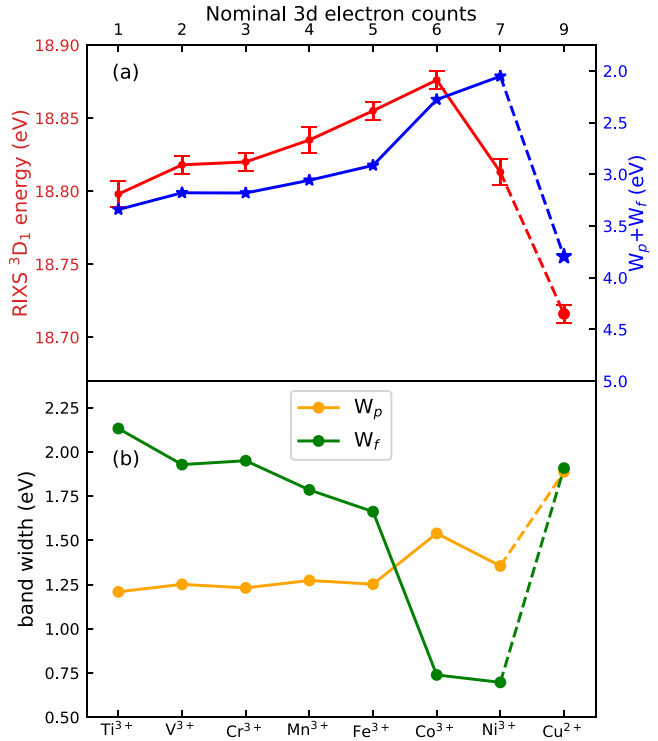

Fig. 4 | Comparison of resonant inelastic X-ray scattering (RIXS) chemical shifts and band widths. a Trends of RIXS energy and bandwidth sum. The error bars are defined as three times the standard errors from the model fits. Note that the axis of the bandwidth sum in blue is plotted inversely. **b** Trends of the La 5p band widths (W_p) and the La 4f band widths (W_f) across the 3d transition metal perovskite oxide series and La_2CuO_4.

Conclusion

Our work demonstrates the direct observation of orbital-overlap-driven La-TM and La-O hybridization via high-resolution RIXS $^3D_1$ final state. By increasing the orbital overlap between TM and La, we increase the band widths and reduce the energy distances of the La 5p-4f transition. The hybridization mechanism of the valence and conduction band is established between La (4f and 5p), TM (partially filled 3d) and O (2p and 2s). With help of DFT calculation, we observe that the 4f bands are getting more localized when increasing TM atomic number, whereas the 5p electrons are getting slightly more delocalized on the La atom in the $LaMO_3$ series. Our investigation provides experimental evidence for the previously hypothesized role of covalency between La and the neighboring ions. The 4f covalency is contributed from hybridization with the TM 3d, whereas the 5p covalency is from the O 2s. Last, we further enhance the radial overlap between La and TM by probing highly covalent layered perovskite La_2CuO_4. An even larger redshift in RIXS $^3D_1$ is achieved by reduced-charge-enhanced ionic radius and the intercalation of La atoms in rock-salt layers. The experimental result suggests that the La atom does not just serve solely as a spacer but electronically contributes to the band formation in perovskite oxides and the parent compound of cuprate superconductors.

Methods

The $N_{4,5}$-edges RIXS experiments were performed at BESSY II (Helmholtz-Zentrum Berlin) at the beamline UE112-PGM1 with the meV-RIXS spectrometer[66] and beamline U49[67] with the SolidFlexRIXS end station[68]. All thin films were grown on $SrTiO_3$ (STO) substrate if not explicitly noted. $LaTiO_3$, $LaVO_3$[69], $LaCrO_3$, $LaFeO_3$ (Nb:STO), $LaCoO_3$ (on STO and $LaAlO_3$ substrates)[70,71], $LaNiO_3$, and La_2CuO_4 (on $LaSrAlO_4$ substrate)[72] thin films were grown by pulsed laser deposition. $LaMnO_3$ thin film was grown by molecular-beam epitaxy. Single crystal $LaCoO_3$ was grown by the floating-zone method[73]. The samples were acquired from the laboratory sources and details about synthesis methods and characterizations can be found in the according references. The RIXS measurements were carried out at room temperature at 10^{-8} mbar pressure with a linearly horizontally polarized beam. The experimental geometry was defined with the incident beam at 30° to the sample surface at a fixed scattering angle of 90° on the horizontal plane. The combined spectral resolution is ≈ 60 meV. Each RIXS spectrum required at least 40 minutes data-acquisition time for sufficient statistical counts.

Calculations were performed using the projector augmented wave scheme as implemented in the VASP code[74–76]. Heyd-Scuseria-Ernzerhof screened hybrid functionals[77] have been employed for $LaMO_3$ with M = Ti-Co and La_2CuO_4. Different values of the mixing parameter have been chosen to better reproduce the experimental band gap. In particular, for $LaMO_3$ we used the values reported in Ref. 41, while we chose $\alpha = 0.25$ for La_2CuO_4. The correlated metal $LaNiO_3$ has been described using the PBE functional[78], as even small corrections open an unphysical band gap[41]. Low temperature, experimental structures[41,79] are used for all compounds. k-point space is sampled with $4 \times 4 \times 4$, $6 \times 6 \times 6$ and $4 \times 4 \times 2$ grids for M = Ti-Fe/M = Ni, M = Co and La_2CuO_4, respectively.

Data availability

Full RIXS datasets collected in this study are available from the corresponding author upon reasonable request.

Received: 26 November 2023; Accepted: 22 April 2024;
Published online: 14 May 2024

References

1. Varignon, J., Grisolia, M. N., Íñiguez, J., Barthélémy, A. & Bibes, M. Complete phase diagram of rare-earth nickelates from first-principles. *npj Quantum Mater.* **2**, 21 (2017).
2. Bisogni, V. et al. Ground-state oxygen holes and the metal-insulator transition in the negative charge-transfer rare-earth nickelates. *Nat. Commun.* **7**, 13017 (2016).
3. Mercy, A., Bieder, J., Íñiguez, J. & Ghosez, P. Structurally triggered metal-insulator transition in rare-earth nickelates. *Nat. Commun.* **8**, 1677 (2017).
4. Hepting, M. et al. Tunable charge and spin order in prnio$_3$ thin films and superlattices. *Phys. Rev. Lett.* **113**, 227206 (2014).
5. Pavarini, E. & Koch, E. Origin of jahn-teller distortion and orbital order in $LaMnO_3$. *Phys. Rev. Lett.* **104**, 086402 (2010).
6. Bhattacharya, D., Devi, P. S. & Maiti, H. S. Orbital order-disorder transition in $La_{1-x}Nd_xMnO_3$ (x = 0.0-1.0) and $La_{1-x-y}Nd_xSr_yMnO_3$ (x = 0.1; y = 0.05,0.1). *Phys. Rev. B* **70**, 184415 (2004).
7. Okamoto, S., Ishihara, S. & Maekawa, S. Phase transition in perovskite manganites with orbital degree of freedom. *Phys. Rev. B* **61**, 14647–14655 (2000).
8. Bednorz, J. G. & Müller, K. A. Perovskite-type oxides—the new approach to high-T_c superconductivity. *Rev. Mod. Phys.* **60**, 585–600 (1988).
9. Keimer, B., Kivelson, S. A., Norman, M. R., Uchida, S. & Zaanen, J. From quantum matter to high-temperature superconductivity in copper oxides. *Nature* **518**, 179–186 (2015).
10. Li, D. et al. Superconductivity in an infinite-layer nickelate. *Nature* **572**, 624–627 (2019).
11. Zhu, H., Zhang, P. & Dai, S. Recent advances of lanthanum-based perovskite oxides for catalysis. *ACS Catal.* **5**, 6370–6385 (2015).
12. Baeumer, C. et al. Tuning electrochemically driven surface transformation in atomically flat $LaNiO_3$ thin films for enhanced water electrolysis. *Nat. Mater.* **20**, 674–682 (2021).
13. Hwang, J. et al. Perovskites in catalysis and electrocatalysis. *Science* **358**, 751–756 (2017).
14. Kostopoulou, A., Kymakis, E. & Stratakis, E. Perovskite nanostructures for photovoltaic and energy storage devices. *J. Mater. Chem. A* **6**, 9765–9798 (2018).
15. Hu, S. et al. Selected multiferroic perovskite oxides containing rare earth and transition metal elements. *Chinese Sci. Bull.* **59**, 5170–5179 (2014).
16. Lone, I. H. et al. Multiferroic ABO_3 transition metal oxides: a rare interaction of ferroelectricity and magnetism. *Nanoscale Res. Lett.* **14**, 142 (2019).
17. Goodenough, J. B. Theory of the role of covalence in the perovskite-type manganites [La, *M*(II)]MnO_3. *Phys. Rev.* **100**, 564–573 (1955).
18. Kanamori, J. Superexchange interaction and symmetry properties of electron orbitals. *J. Phys. Chem. Solids* **10**, 87–98 (1959).
19. Bouarab, S., Vega, A. & Khan, M. A. Ab initio optical conductivity in $LaMO_3$ (M = Ti-Cu). *Phys. Rev. B* **54**, 11271–11275 (1996).
20. Kim, B., Liu, P., Tomczak, J. M. & Franchini, C. Strain-induced tuning of the electronic coulomb interaction in 3*d* transition metal oxide perovskites. *Phys. Rev. B* **98**, 075130 (2018).
21. Frati, F., Hunault, M. O. & De Groot, F. M. Oxygen K-edge X-ray absorption spectra. *Chem. Rev.* **120**, 4056–4110 (2020).
22. Alonso, J. A., Martínez-Lope, M. J., Casais, M. T., García-Muñoz, J. L. & Fernández-Díaz, M. T. Room-temperature monoclinic distortion due to charge disproportionation in $RNiO_3$ perovskites with small rare-earth cations (*R* = Ho, Y, Er, Tm, Yb, and Lu): a neutron diffraction study. *Phys. Rev. B* **61**, 1756–1763 (2000).
23. Prosandeev, S., Bellaiche, L. & Íñiguez, J. Ab initio study of the factors affecting the ground state of rare-earth nickelates. *Phys. Rev. B* **85**, 214431 (2012).
24. Kim, M. W. et al. Effect of orbital rotation and mixing on the optical properties of orthorhombic $RMnO_3$ (*R* = La, Pr, Nd, Gd, and Tb). *Phys. Rev. Lett.* **96**, 247205 (2006).
25. Petit, L., Svane, A., Szotek, Z. & Temmerman, W. M. First-principles study of rare-earth oxides. *Phys. Rev. B* **72**, 205118 (2005).
26. El-Kelany, K. E. et al. Spin localization, magnetic ordering, and electronic properties of strongly correlated Ln_2O_3 sesquioxides (Ln = La, Ce, Pr, Nd). *Phys. Rev. B* **97**, 245118 (2018).
27. Hepting, M. et al. Electronic structure of the parent compound of superconducting infinite-layer nickelates. *Nat. Mater.* **19**, 381–385 (2020).
28. Löble, M. W. et al. Covalency in Lanthanides. An X-ray Absorption Spectroscopy and Density Functional Theory Study of $LnCl_6^{x-}$ (x = 3, 2). *J. Am. Chem. Soc.* **137**, 2506–2523 (2015).
29. Peng, C., Jiang, H.-C., Moritz, B., Devereaux, T. P. & Jia, C. Charge order and superconductivity in a two-band model for infinite-layer nickelates. *Phys. Rev. B* **108**, 245115 (2023).
30. Tam, C. C. et al. Charge density waves in infinite-layer $NdNiO_2$ nickelates. *Nat. Mater.* **21**, 1116–1120 (2022).
31. Jiang, P., Si, L., Liao, Z. & Zhong, Z. Electronic structure of rare-earth infinite-layer $RNiO_2$(*R* = La, Nd). *Phys. Rev. B* **100**, 201106 (2019).
32. Zhang, R. et al. Magnetic and f-electron effects in $LaNiO_2$ and $NdNiO_2$ nickelates with cuprate-like $3d_{x^2-y^2}$ band. *Commun. Phys*. **4**, 118 (2021).
33. Pan, G. A. et al. Superconductivity in a quintuple-layer square-planar nickelate. *Nat. Mater.* **21**, 160–164 (2022).
34. Liu, T. et al. Dimensionality-induced insulator-metal crossover in layered nickelates $La_{n+1}Ni_nO_{2n+2}$ (n = 2, 3, and ∞). *AIP Adv*. **4** 047132 (2014).
35. Wang, L. et al. Tuning bifunctional oxygen electrocatalysts by changing the a-site rare-earth element in perovskite nickelates. *Adv. Funct. Mater.* **28**, 1803712 (2018).
36. Been, E. et al. Electronic structure trends across the rare-earth series in superconducting infinite-layer nickelates. *Phys. Rev. X* **11**, 011050 (2021).
37. Lee, K.-W. & Pickett, W. E. Infinite-layer $LaNiO_2$: Ni^{1+} is not Cu^{2+}. *Phys. Rev. B* **70**, 165109 (2004).
38. Gu, Y., Zhu, S., Wang, X., Hu, J. & Chen, H. A substantial hybridization between correlated Ni-d orbital and itinerant electrons in infinite-layer nickelates. *Commun. Phys.* **3**, 84 (2020).
39. Higashi, K., Winder, M., Kuneš, J. & Hariki, A. Core-level x-ray spectroscopy of infinite-layer nickelate: LDA + DMFT study. *Phys. Rev. X* **11**, 041009 (2021).
40. Pari, G., Mathi Jaya, S., Subramoniam, G. & Asokamani, R. Density-functional description of the electronic structure of $LaMO_3$ (M = Sc,Ti,V,Cr,Mn,Fe,Co,Ni). *Phys. Rev. B* **51**, 16575–16581 (1995).
41. He, J. & Franchini, C. Screened hybrid functional applied to $3d^0 \rightarrow 3d^8$ transition-metal perovskites $LaMO_3$ (*M* = Sc–Cu): Influence of the exchange mixing parameter on the structural, electronic, and magnetic properties. *Phys. Rev. B* **86**, 235117 (2012).
42. May, K. J. & Kolpak, A. M. Improved description of perovskite oxide crystal structure and electronic properties using self-consistent Hubbard *U* corrections from ACBN0. *Phys. Rev. B* **101**, 165117 (2020).
43. Franchini, C. Hybrid functionals applied to perovskites. *J. Phys. Condens. Matter* **26**, 253202 (2014).
44. Varrassi, L. et al. Optical and excitonic properties of transition metal oxide perovskites by the bethe-salpeter equation. *Phys. Rev. Mater.* **5**, 074601 (2021).
45. Ergönenc, Z., Kim, B., Liu, P., Kresse, G. & Franchini, C. Converged *GW* quasiparticle energies for transition metal oxide perovskites. *Phys. Rev. Mater.* **2**, 024601 (2018).
46. Zaanen, J., Sawatzky, G. A. & Allen, J. W. Band gaps and electronic structure of transition-metal compounds. *Phys. Rev. Lett.* **55**, 418–421 (1985).

47. Suntivich, J. et al. Estimating Hybridization of Transition Metal and Oxygen States in Perovskites from O K-edge X-ray Absorption Spectroscopy. *J. Phys. Chem. C* **118**, 1856–1863 (2014).
48. de Groot, F. M. F. et al. Oxygen 1s x-ray-absorption edges of transition-metal oxides. *Phys. Rev. B* **40**, 5715–5723 (1989).
49. Walters, A. C. et al. Effect of covalent bonding on magnetism and the missing neutron intensity in copper oxide compounds. *Nat. Phys.* **5**, 867–872 (2009).
50. Ament, L. J., Van Veenendaal, M., Devereaux, T. P., Hill, J. P. & Van Den Brink, J. Resonant inelastic x-ray scattering studies of elementary excitations. *Rev. Mod. Phys.* **83**, 705–767 (2011).
51. Gilmore, K. et al. Description of resonant inelastic x-ray scattering in correlated metals. *Phys. Rev. X* **11**, 031013 (2021).
52. Mitrano, M. & Wang, Y. Probing light-driven quantum materials with ultrafast resonant inelastic x-ray scattering. *Commun. Phys.* **3**, 184 (2020).
53. Huang, H. Y. et al. Resonant inelastic X-ray scattering as a probe of J_{eff} = 1/2 state in 3d transition-metal oxide. *npj Quantum Mater.* **7**, 33 (2022).
54. Kotani, A. & Shin, S. Resonant inelastic x-ray scattering spectra for electrons in solids. *Rev. Mod. Phys.* **73**, 203–246 (2001).
55. Schülke, W. *Electron Dynamics by Inelastic X-Ray Scattering* 7 edn. (Oxford University Press, 2007).
56. Liu, C.-Y. et al. Role of La 5p in bulk and quantum-confined solids probed by the La $5p^5 4f^{13} D_1$ excitonic final state of resonant inelastic X-ray scattering. *J. Phys. Chem. C* **127**, 11111–11118 (2023).
57. Suljoti, E. et al. Spin-Orbit mediated interference in the radiative and nonradiative channels of the La 4*d* core resonances. *Phys. Rev. Lett.* **103**, 137401 (2009).
58. Moewes, A., Postnikov, A. V., Kurmaev, E. Z., Grush, M. M. & Ederer, D. L. Resonant mixing of widely separated intermediate states and charge transfer at the 4d-4f resonance of La compounds. *Europhys. Lett.* **49**, 665–671 (2000).
59. Epstein, G. L. & Reader, J. Spectrum and energy levels of triply ionized lanthanum (La iv). *J. Opt. Soc. Am.* **69**, 511 (1979).
60. Shannon, R. D. Revised effective ionic radii and systematic studies of interatomic distances in halides and chalcogenides. *Acta Crystallogr. Sect. A* **32**, 751–767 (1976).
61. Manthiram, A. A reflection on lithium-ion battery cathode chemistry. *Nat. Commun.* **11**, 1550 (2020).
62. Vitova, T., Roesky, P. W. & Dehnen, S. Open questions on bonding involving lanthanide atoms. *Commun. Chem.* **5**, 12 (2022).
63. Lu, E. et al. Emergence of the structure-directing role of f-orbital overlap-driven covalency. *Nat. Commun.* **10**, 634 (2019).
64. Zhang, L. et al. Strong-correlated behavior of 4f electrons and 4f5d hybridization in PrO2. *Sci. Rep.* **8**, 1–8 (2018).
65. Nohara, Y., Yamamoto, S. & Fujiwara, T. Electronic structure of perovskite-type transition metal oxides $LaMO_3$(M = Ti ~ Cu) by U + GW approximation. *Phys. Rev. B* **79**, 195110 (2009).
66. Bauer, K. et al. The meV XUV-RIXS facility at UE112-PGM1 of BESSY II. *J. Synchrotron Radiat.* **29**, 908–915 (2022).
67. Kachel, T. The plane grating monochromator beamline U49-2 PGM-1 at BESSY II. *J. Large-scale Res. Facil. JLSRF* **2**, A72 (2016).
68. Beye, M. & Miedema, P. S. Solid flexRIXS: A RIXS endstation for solid systems at BESSY II. *J. Large-scale Res. Facil. JLSRF* **3**, A124 (2017).
69. Ruotsalainen, K. et al. Resonant inelastic x-ray scattering study of doping and temperature dependence of low-energy excitations in $La_{1-x}Sr_xVO_3$ thin films. *Phys. Rev. B* **103**, 235158 (2021).
70. Wang, R.-P. et al. Low-energy orbital excitations in strained $LaCoO_3$ films. *Phys. Rev. B* **100**, 165148 (2019).
71. Hariki, A. et al. Damping of spinful excitons in $LaCoO_3$ by thermal fluctuations: Theory and experiment. *Phys. Rev. B* **101**, 245162 (2020).
72. Martinelli, L. et al. Collective Nature of Orbital Excitations in Layered Cuprates in the Absence of Apical Oxygens. *Phys. Rev. Lett.* **132**, 066004 (2024).
73. Tomiyasu, K. et al. Coulomb Correlations Intertwined with Spin and Orbital Excitations in $LaCoO_3$. *Phys. Rev. Lett.* **119**, 196402 (2017).
74. Kresse, G. & Hafner, J. Ab initio molecular dynamics for liquid metals. *Phys. Rev. B* **47**, 558–561 (1993).
75. Kresse, G. & Furthmüller, J. Efficient iterative schemes for ab initio total-energy calculations using a plane-wave basis set. *Phys. Rev. B* **54**, 11169–11186 (1996).
76. Kresse, G. & Joubert, D. From ultrasoft pseudopotentials to the projector augmented-wave method. *Phys. Rev. B* **59**, 1758–1775 (1999).
77. Krukau, A. V., Vydrov, O. A., Izmaylov, A. F. & Scuseria, G. E. Influence of the exchange screening parameter on the performance of screened hybrid functionals. *J. Chem. Phys.* **125**, 224106 (2006).
78. Perdew, J. P., Burke, K. & Ernzerhof, M. Generalized gradient approximation made simple. *Phys. Rev. Lett.* **77**, 3865–3868 (1996).
79. Jorgensen, J. D. et al. Superconducting phase of $La_2CuO_{4+\delta}$: A superconducting composition resulting from phase separation. *Phys. Rev. B* **38**, 11337–11345 (1988).
80. Ivashko, O. et al. Strain-engineering mott-insulating La_2CuO_4. *Nat. Commun.* **10**, 786 (2019).

Acknowledgements

We are grateful for the awarded beamtimes at BESSY II operated by the Helmholtz-Zentrum Berlin für Materialien und Energie. K.S. thanks the Humboldt Foundation for funding from the Humboldt Research Fellowship for postdoctoral researchers program. L.C. acknowledges the Vienna Doctoral School of Physics. The computational results have been achieved using the Vienna Scientific Cluster (VSC). M.L. and F.d.G. received funding from the European Union's Horizon 2020 research and innovation programme under the Marie Skłodowska-Curie grant agreement No 860553.

Author contributions

C.-Y.L. and A.F. conceptualized the project. L.C. performed theoretical calculations. C.-Y.L., K.R., K.S., M.K., R.D., K.N.P., and M.L. planned and performed the experiments. R-P.W., I.I.O., D.J.K., D.D.C., K.T., E.M., Y.A.B., E.M.K., I.C.G.B., and M.L. prepared and synthesized the samples. C.B., G.K. and C.D. supervised the PLD/MBE synthesis and laboratory-based characterization methods. C.-Y.L. analyzed the experimental data. F.d.G., C.F. supervised theoretical interpretation. C.-Y.L., L.C., R.D., K.R., Y.A.B., C.B. and A.F. wrote the manuscript with input from all the authors.

Funding

Open Access funding enabled and organized by Projekt DEAL.

Competing interests

The authors declare no competing interests.

Additional information

Supplementary information The online version contains supplementary material available at https://doi.org/10.1038/s42005-024-01642-5.

Correspondence and requests for materials should be addressed to Chun-Yu Liu or Alexander Föhlisch.

Peer review information *Communications Physics* thanks Clemens Ulrich and the other, anonymous, reviewer(s) for their contribution to the peer review of this work.